Transient Prediction of Radiation Response in a 3-D Scattering-Absorbing Medium Subjected to a Collimated Short Square Pulse Train

Masato Akamatsu [a] & Zhixiong Guo [b]

[a] Graduate School of Science and Engineering, Yamagata University, Yamagata, Japan

[b] Department of Mechanical and Aerospace Engineering, Rutgers, The State University of New Jersey, Piscataway, New Jersey, USA
Version of record first published: 21 Dec 2012.

PLEASE SCROLL DOWN FOR ARTICLE

Taylor & Francis
Taylor & Francis Group

TRANSIENT PREDICTION OF RADIATION RESPONSE IN A 3-D SCATTERING-ABSORBING MEDIUM SUBJECTED TO A COLLIMATED SHORT SQUARE PULSE TRAIN

Masato Akamatsu[1] and Zhixiong Guo[2]

[1]*Graduate School of Science and Engineering, Yamagata University, Yamagata, Japan*

[2]*Department of Mechanical and Aerospace Engineering, Rutgers, The State University of New Jersey, Piscataway, New Jersey, USA*

Transient radiative transfer characteristics in a three-dimensional scattering-absorbing medium subjected to collimated irradiation of a short pulse train were investigated. A basic problem in which a cube is exposed to collimated irradiation of a single unit step square pulse was solved via the transient discrete-ordinates method, and Duhamel's superposition theorem was used to construct the responses of various pulse trains. The effects of optical thickness, scattering albedo, pulse width, and pulse train interval between two successive pulses on the temporal profiles of divergence of radiative heat flux, reflectance, and transmittance were scrutinized.

INTRODUCTION

The advent of ultra-short pulsed lasers with pulse widths on the order of femtoseconds to picoseconds has attracted increasing attention for potential use in processing, treatment, diagnostics of biological tissues [1–10], and photonic crystals [11]. Regarding the application of such ultra-short pulsed lasers to medical imaging techniques, the development of optical computed tomography (optical-CT or OCT) has been proceeding vigorously, as optical-CT is expected to provide imaging information about both physiology and morphology inside living bodies [2–5]. X-ray CT and magnetic resonance imaging (MRI) are currently used extensively in the medical field, but these modalities mainly provide information about morphology inside living bodies. It is noticed that functional-MRI is in development, yet the facility size and cost associated with MRI are not comparable with optical technology. To enable fully-functional Optical-CT, clarification is needed with regard to the transient radiative transfer characteristics of scattered signals induced by the interaction of pulsed light in highly scattering and weakly absorbing biological tissues.

NOMENCLATURE

c	speed of light in medium, m/s	x^*	nondimensional coordinate in x direction $= x/L$
d_c	width of the collimated laser sheet, m	y^*	nondimensional coordinate in y direction $= y/L$
G	incident radiation, W/m^2	z^*	nondimensional coordinate in z direction $= z/L$
I	radiation intensity, W/m$^2 \cdot$ sr		
I_c	laser intensity, W/m^2	δ	Dirac delta function
L	length, m	Δt	time step, s
N	angular discrete order in S_N approximation	$\Delta x, \Delta y, \Delta z$	grid size, m
n	number of angular discretization	Φ	scattering phase function
Q	net radiative heat flux, W/m^2	η, μ, ξ	direction cosines
$\vec{q}$	radiative heat flux, W/m^2	ρ	diffuse reflectivity
R	reflectance	σ_a	absorption coefficient, 1/m
$\vec{r}$	position vector, m	σ_e	extinction coefficient, 1/m
S	source term, W/m^2	σ_s	scattering coefficient, 1/m
$\hat{s}$	discrete ordinate direction	ω	scattering albedo
T	transmittance		
t	time, s	**Subscripts**	
t^*	nondimensional time $= ct/L$	b	blackbody
t_d	pulse train interval between two successive pulses, s	c	collimated laser
		w	wall
t_p	pulse width, s		
w	angular weight	**Superscripts**	
x, y, z	Cartesian coordinates, m	l	discrete direction index
		$*$	dimensionless quantity

Various numerical methods including the P-approximation [12], the Monte Carlo method [13, 14], discrete-ordinates method (DOM) [15, 16], method of lines (MOL) solution of DOM [17], and the finite-volume method [18, 19] have been developed for modeling the ultrafast radiative transfer in absorbing and scattering media. Other noticeable reports on radiative transfer modeling of a collimated short pulse irradiation with step and Gaussian temporal profiles in a participating medium include Mitra and Kumar [20], Guo and Kumar [21], Kim and Guo [22], Wu and Ou [23], Mishra et al. [24], and Okutucu and Yener [25]. In all these studies, the emphasis of the investigations was placed on the transport of a single ultra-short pulse. In reality, however, continuous pulse trains are usually applied. An investigation of the transport of ultra-short pulse trains is expected to provide more useful information about transient radiative transfer characteristics in participating media.

In relation to numerical computations with a pulse train, both one-dimensional and two-dimensional simulations were implemented by Muthukumaran and Mishra [26–29] for homogeneous and inhomogeneous participating media. A literature survey revealed no three-dimensional simulation work on the effect of a pulse train, and thus, the present authors conducted three-dimensional simulation on the interaction of diffuse irradiation of a square pulse train in a highly scattering cube [30].

The irradiation of lasers is actually ballistic (either collimated or focused), rather than diffuse. The difference of beam-splitting treatment and results between collimated and diffuse radiation is appreciable [7]. To this end, the present three-dimensional simulation work is aimed at the clarification of the transient characteristics of ultrafast

laser radiative transfer in strongly scattering and weakly absorbing media subjected to collimated irradiation of various square pulse trains. The effects of various pulse widths and various time intervals between pulses are examined.

GOVERNING EQUATIONS

The model system used in the present computations is shown in Figure 1. The collimated laser sheet directed normal to the wall is incident at the center of the wall at $x = 0$ with a width of d_c. The spatial width of the incident laser sheet is $d_c = L/49$, whose temporal variation is a step function. Detectors 1 and 2 are located at the wall of $x = 0$ with $y = z = L/2$ and $y = L/2$, $z = L/4$, respectively, to detect the reflectance signals. Detectors 3 and 4 are located at the opposite wall of $x = L$ with $y = z = L/2$ and $y = L/2$, $z = L/4$, respectively, to detect the transmittance signals. The cubic homogeneous medium is cold (non-emitting), strongly scattering and weakly absorbing.

The transient equations of diffuse radiative transfer in discrete ordinates can be formulated as follows.

$$\frac{1}{c}\frac{\partial I^l}{\partial t} + \xi^l\frac{\partial I^l}{\partial x} + \eta^l\frac{\partial I^l}{\partial y} + \mu^l\frac{\partial I^l}{\partial z} + \sigma_e I^l = \sigma_e S^l \qquad l = 1, 2, \cdots, n \qquad (1)$$

The extinction coefficient σ_e is the summation of the absorption coefficient σ_a and scattering coefficient σ_s. The scattering albedo is $\omega = \sigma_s/\sigma_e$. S^l is the radiative source term, neglecting blackbody emission. It can be expressed as follows.

$$S^l = \frac{\omega}{4\pi}\sum_{i=1}^{n} w^i \Phi^{il} I^i + S_c^l \qquad l = 1, 2, \cdots, n \qquad (2)$$
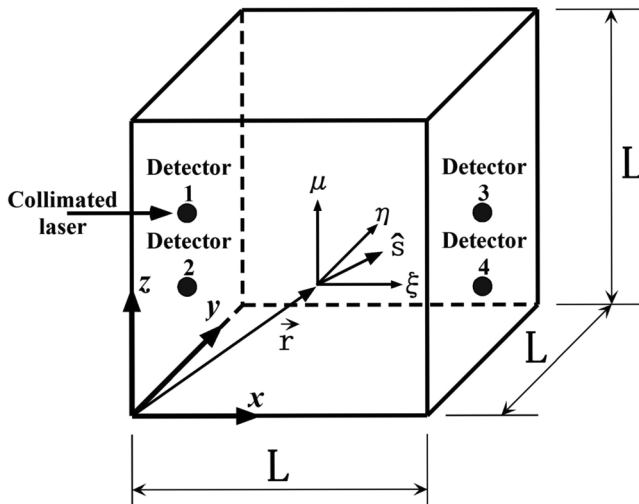

Figure 1. Three-dimensional geometry and coordinates system.

The first term on the right-hand side in Eq. (2) is the contribution of in-scattering radiation intensities from all discrete ordinate directions. The second term is the source contribution of the collimated laser irradiation, which is the driving force of the scattered radiation propagation and transport in the medium.

$$S_c^l = \frac{\omega}{4\pi} I_c \Phi\left(\xi^c \xi^l + \eta^c \eta^l + \mu^c \mu^l\right) \tag{3}$$

Where (ξ^c, η^c, μ^c) represents the collimated laser incident direction. In the present model, $\xi^c = 1$, $\eta^c = 0$, and $\mu^c = 0$, since the collimated laser is normally incident at the wall at $x = 0$, as shown in Figure 1.

The collimated laser intensity (heat flux) is distributed inside the medium as follows.

$$I_c(x, y, z, \xi^c, t) = I_0\left(x = 0, y = z = \frac{L}{2}, t - \frac{x}{c\xi^c}\right) e^{-\frac{\sigma_e x}{\xi^c}} \delta(\xi^c - 1) \tag{4}$$

In which δ is the Dirac delta function and I_0 is the laser beam heat flux irradiated into the surface of the medium (surface reflection is deducted). In the region where no collimated laser irradiation passes through, $I_c = S_c = 0$.

A quadrature set of the DOM S_N-approximation include n discrete ordinates with appropriate angular weight, in which $n = N(N + 2)$. In the present computations, S_{12}-approximation is applied for obtaining the solution for the basic problem with a unit step pulse. Here, $\Phi(\hat{s}^i \rightarrow \hat{s}^l)$ is the scattering phase function. In the present study, the scattering is assumed isotropic or scaled isotropic [31].

The walls are assumed to be gray and diffusely reflecting. For example, the diffuse intensity at the wall of $x = 0$ is as follows.

$$I_w = (1 - \rho)I_{bw} + \frac{\rho}{\pi} \sum_{\xi^l < 0}^{n/2} w^l I^l |\xi^l| \tag{5}$$

Where I_w is the diffuse intensity at the wall, I_{bw} is the blackbody intensity at the wall, ρ is the diffuse reflectivity of the wall surface, and $n/2$ is denoted that half of the n different intensities emanate from the wall. Similarly, the relationships for the remaining five walls can be set up. In the case of $\rho = 0$, the sidewalls are black and absorb all incident radiation.

Once the intensities have been determined, the net radiative heat flux Q_x, Q_y, and Q_z and the incident radiation G are evaluated from the following.

$$Q_x = \sum_{l=1}^{n} \xi^l w^l I^l + I_c, \quad Q_y = \sum_{l=1}^{n} \eta^l w^l I^l, \quad Q_z = \sum_{l=1}^{n} \mu^l w^l I^l \tag{6}$$

$$G = \sum_{l=1}^{n} w^l I^l + I_c \tag{7}$$

The divergence of the total heat flux for nonemitting media is obtained by the following.

$$\nabla \cdot \vec{q} = -(1 - \omega) \cdot \sigma_e \cdot G \tag{8}$$

The transient reflectance at $x = 0$ and the transient transmittance at the opposite output wall of $x = L$ for the basic problem are defined as follows.

$$R(x = 0, y, z, t) = \frac{Q_x(x = 0, y, z, t) - I_c(x = 0, y, z, t)}{I_0} \tag{9}$$

$$T(x = L, y, z, t) = \frac{Q_x(x = L, y, z, t)}{I_0} \tag{10}$$

NUMERICAL SCHEME

In our previous numerical investigation [30], we examined the influences of the spatial grid and time step on the temporal profiles of reflectance and transmittance to minimize the effects of false radiation propagation and numerical diffusion for solving ultrafast radiative transfer in a highly scattering medium, and the optimum spatial grid and time step were decided. In the present numerical computations, the spatial grid and time step determined in the previous study were also adopted. Namely, the spatial grid number and the time step were $49 \times 49 \times 49$ and $\Delta t^* = 0.006$, respectively.

The control volume approach is used for the spatial discretization to solve the transient radiation transfer equation, i.e., Eq. (1). In each control volume, Eq. (1) is discretized temporally and spatially. The final discretization equation for the cell intensity in a generalized form [15] becomes the following.

$$I_P^l = \frac{\frac{1}{c\Delta t}I_p^{l0} + \sigma_e S_p^l + \frac{|\xi^l|}{\gamma_x^l \Delta x}I_{xu}^l + \frac{|\eta^l|}{\gamma_y^l \Delta y}I_{yu}^l + \frac{|\mu^l|}{\gamma_z^l \Delta z}I_{zu}^l}{\frac{1}{c\Delta t} + \sigma_e + \frac{|\xi^l|}{\gamma_x^l \Delta x} + \frac{|\eta^l|}{\gamma_y^l \Delta y} + \frac{|\mu^l|}{\gamma_z^l \Delta z}} \tag{11}$$

Where I_p is the intensity at the node of a control volume; I_p^{l0} is the intensity at previous time step; and I_{xu}^l, I_{yu}^l, and I_{zu}^l are the radiation intensities on the upstream surface in the $\hat{s}^l$ direction. In the present method the positive scheme proposed by Lathrop [32] is applied to determine the values of weighting factors γ_x^l, γ_y^l, and γ_z^l. With the nodal intensity obtained from Eq. (11), the unknown radiation intensities on the downstream surface in the same direction are computed as follows.

$$I_p^l = \gamma_x^l I_{xd}^l + (1 - \gamma_x^l)I_{xu}^l = \gamma_y^l I_{yd}^l + (1 - \gamma_y^l)I_{yu}^l = \gamma_z^l I_{zd}^l + (1 - \gamma_z^l)I_{zu}^l \tag{12}$$

Where I_{xd}^l, I_{yd}^l, and I_{zd}^l are the radiation intensities on the downstream surface in the $\hat{s}^l$ direction.

In Eq. (11), the traveling distance $c\Delta t$ should not exceed the control volume spatial step, i.e., $c\Delta t < \min\{\Delta x, \Delta y, \Delta z\}$. This is because a light beam always travels at the speed of light c in the medium. Hence, the following condition is imposed to eliminate the numerical diffusion [21].

$$\Delta t^* < \min\{\Delta x^*, \Delta y^*, \Delta z^*\} \tag{13}$$

The present method was verified by comparing the existing published results and/or with the Monte Carlo simulation for a variety of example problems in two- and three-dimensional systems [15, 21]. It was found that the present method was accurate and efficient.

RESULTS AND DISCUSSION

Figure 2 shows the effects of medium optical thickness and scattering albedo on the temporal profiles of the divergence of radiative heat flux at $x^* = y^* = z^* = 0.5$ (the center of the cube) in a unit cube subjected to a single collimated unit step square pulse. Two scattering albedo values ($\omega = 0.95$ and 0.90) were considered. The diffuse reflectivity ρ was assumed to be zero. The increase of the optical thickness implies an increase of the extinction coefficient of the medium. For the same optical thickness, the increase of the scattering albedo implies an increase of the scattering coefficient and a decrease of the absorption coefficient. It is seen that as time proceeds, the divergence of radiative heat flux for the three different optical thicknesses increases quickly at about $t^* = 0.5$ and reaches constant values.
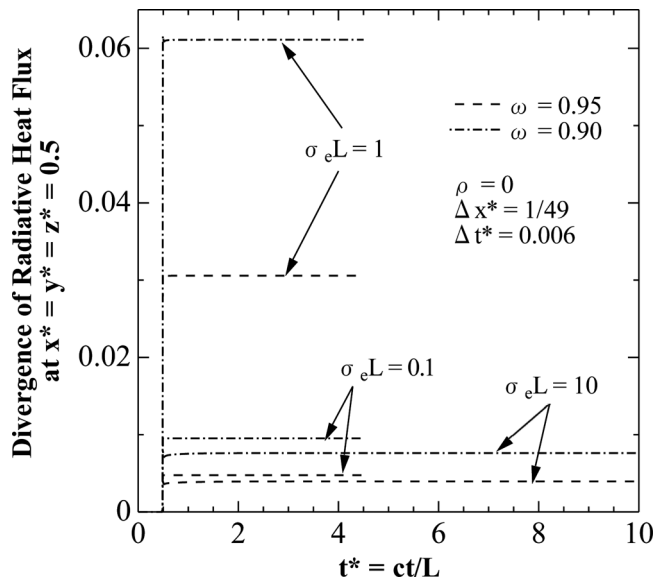

Figure 2. Effects of optical thickness and scattering albedo on the temporal profiles of the divergence of radiative heat flux at $x^* = y^* = z^* = 0.5$ in a unit cube subjected to a single collimated unit step square pulse.

Figure 3 provides the contour plots of divergence of radiative heat flux drawn at every 0.0001 between 0 and 0.01 in the X-Z plane at $y^* = 0.5$ in the steady state (long time stage). The figure shows six cases: (a) $\sigma_e L = 0.1$, $\omega = 0.9$, (b) $\sigma_e L = 0.1$, $\omega = 0.95$, (c) $\sigma_e L = 1$, $\omega = 0.9$, (d) $\sigma_e L = 1, \omega = 0.95$, (e) $\sigma_e L = 10$, $\omega = 0.9$, and (f) $\sigma_e L = 10, \omega = 0.95$, respectively. Since the finite volume elements have nodes at the centers of the elements, these figures are drawn in the volume $\frac{1}{49} \leq x^*, y^*, z^* \leq \frac{48}{49}$. The numerical value with the arrow in the figure shows the value of divq at $x^* = y^* = z^* = 0.5$ (the center of the cube). The divergence of radiative heat flux translates to the energy deposition rate. It is seen that the divergence of radiative heat flux is greatly concentrated near the collimated laser-incident spot, the increase of the optical thickness enhances the energy deposition, and the increase of the scattering albedo decreases the energy deposition. Although the magnitude of divq for $\sigma_e L = 0.1$ and 1 gradually decreases with the increase of the x position, that for
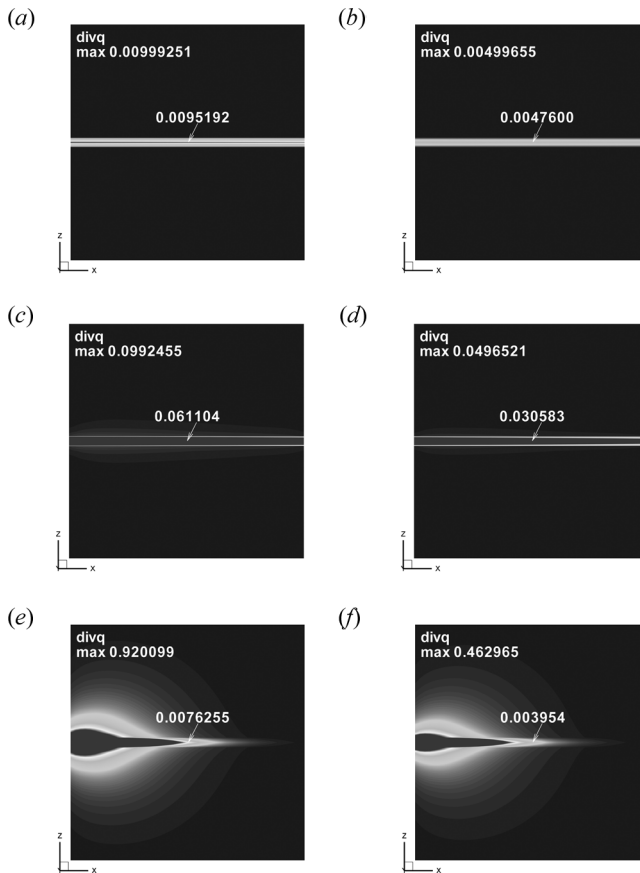

Figure 3. Contour plots of divergence of radiative heat flux drawn at every 0.0001 between 0 and 0.01 in X-Z plane at $y^* = 0.5$ in the steady state. (a) $\sigma_e L = 0.1$, $\omega = 0.9$, (b) $\sigma_e L = 0.1$, $\omega = 0.95$, (c) $\sigma_e L = 1$, $\omega = 0.9$, (d) $\sigma_e L = 1$, $\omega = 0.95$, (e) $\sigma_e L = 10$, $\omega = 0.9$, and (f) $\sigma_e L = 10$, $\omega = 0.95$.

$\sigma_e L = 10$ decreases dramatically. Namely, the depth of the energy deposition for optically thick medium is much shallower than that for optically thin medium. Hence, we see that the constant values of the divergence of radiative heat flux at the long time stage for $\sigma_e L = 1$ become much larger than those for $\sigma_e L = 10$, and those for $\sigma_e L = 10$ become almost the same as those for $\sigma_e L = 0.1$ with the absorption coefficient of $1/100$ times of $\sigma_e L = 10$ for the same scattering albedo as shown in Figure 2. Since the absorption coefficient of $\omega = 0.95$ is half of that of $\omega = 0.9$, the magnitude of div$q$ for $\omega = 0.95$ becomes about half of that for $\omega = 0.9$ for the same optical thickness as shown by the numerical value with the arrow. Therefore, the difference between the constant values of the divergence of radiative heat flux for $\sigma_e L = 1, \omega = 0.9$ and $\sigma_e L = 1, \omega = 0.95$ becomes much larger than those for $\sigma_e L = 0.1$ and 1 relatively.
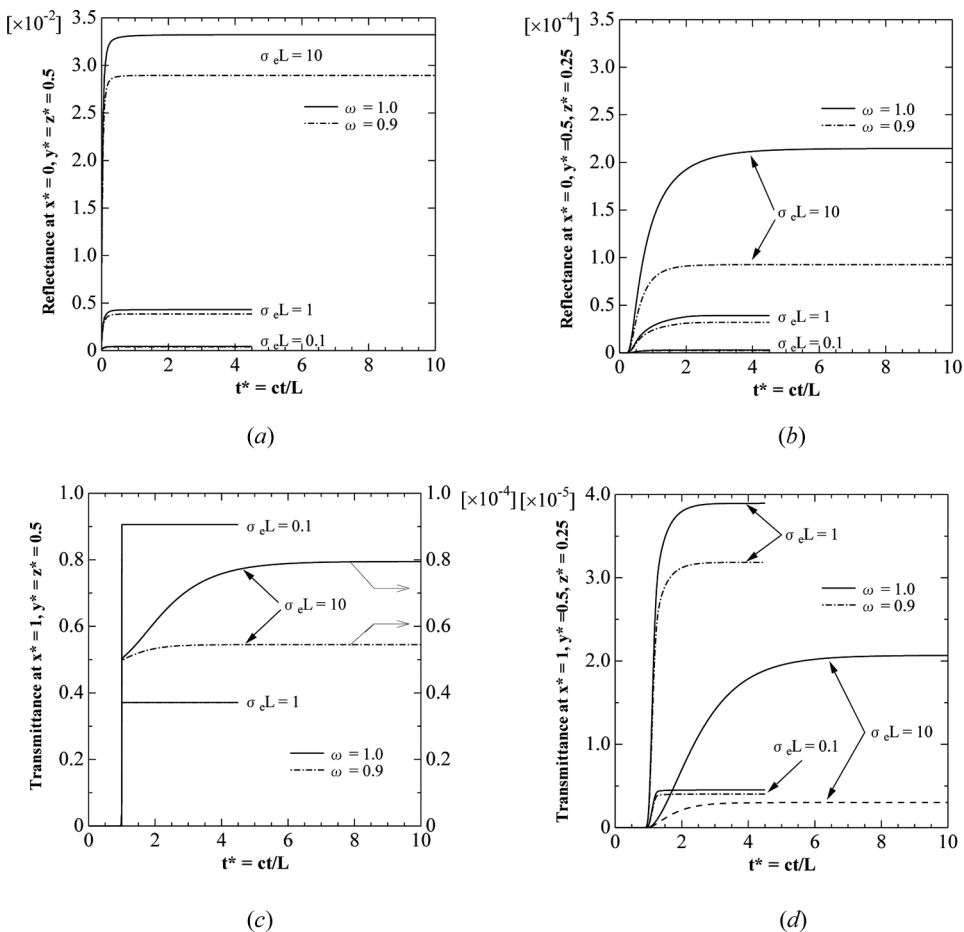

Figure 4. Effects of optical thickness and scattering albedo on the temporal profiles of (*a*) and (*b*) reflectance detected by detectors 1 and 2, respectively, and (*c*) and (*d*) transmittance detected by detectors 3 and 4, respectively, when the spot at $x^* = 0$, $y^* = z^* = 0.5$ is subjected to a single collimated unit step square pulse.

Figure 4 shows the effects of optical thickness and scattering albedo on the temporal profiles of reflectance detected by detectors 1 and 2, and transmittance detected by detectors 3 and 4, respectively, when the spot at $x^* = 0$, $y^* = z^* = 0.5$ is subjected to a single collimated unit step square pulse. In Figure 4, it is seen that the reflectance and transmittance signals reach constant values, and these temporal developments are extended significantly as the optical thickness increases. At the locations of detectors 3 and 4, the transmittance signals remain zero until about $t^* = 1$. This is because $t^* = 1$ is exactly the shortest flight time of light passing through the medium without interaction with the medium. In Figures 4a and 4b, it is seen that the reflectance signals detected by detectors 1 and 2 increase drastically as the optical thickness increases. Similarly, the scattering albedo's increase is magnified
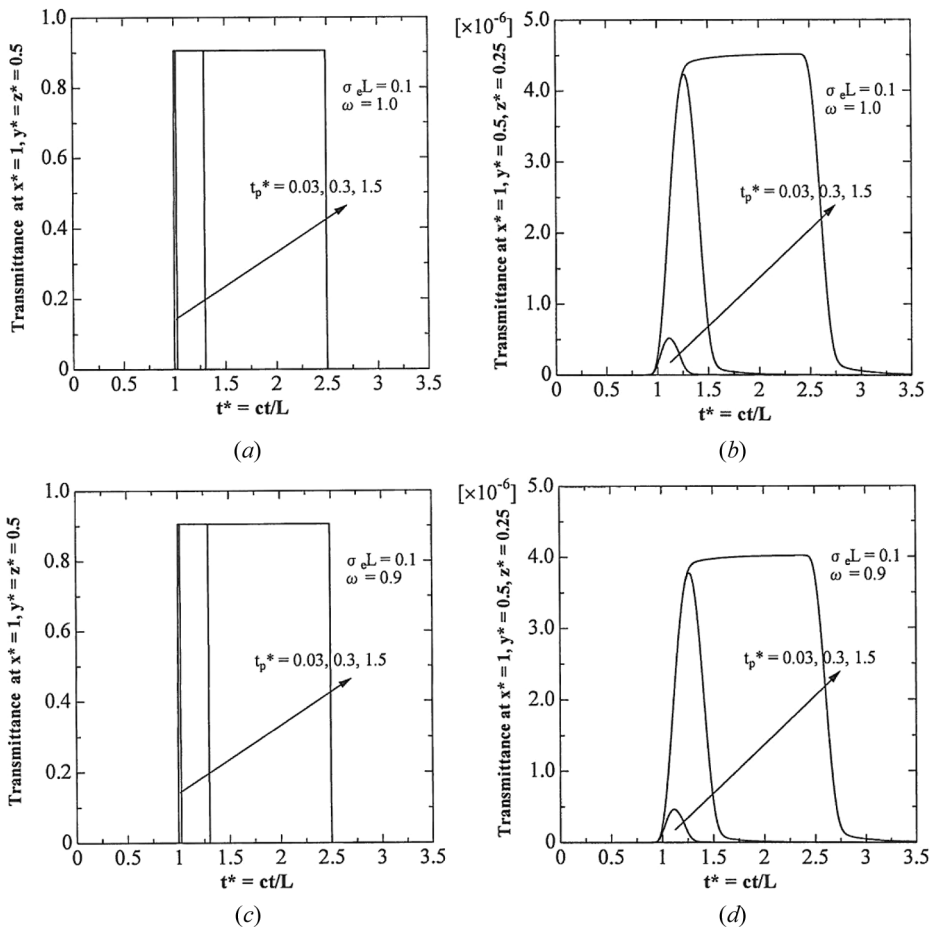

Figure 5. Temporal distributions of transmittance at detectors 3 and 4 for (a) and (b) $\sigma_e L = 0.1$, $\omega = 1$, and (c) and (d) $\sigma_e L = 0.1$, $\omega = 0.9$, when the spot at $x^* = 0$, $y^* = z^* = 0.5$ of the unit cube is subjected to a single collimated square pulse with various pulse widths of $t_p^* = 0.03$, 0.3, and 1.5.

the reflectance for the same optical thickness. In contrast, Figure 4*c* shows that the transmittance signal at detector 3 decreases dramatically as the optical thickness increases (see the left ordinate for $\sigma_e L = 0.1$, 1 and the right ordinate for $\sigma_e L = 10$). The increase of scattering albedo increases the magnitude of transmittance for the same optical thickness. In Figure 4*d*, we see that the transmittance signal at detector 4 show different behaviors in relation to the change of optical thickness in comparison with the trend of those shown by detector 3. Initially, we inferred that the transmittance detected by detector 4 increases with the increase of optical thickness because of the increase of the scattering coefficient. However, as a result, we suspect that different behaviors, as shown in Figure 4*d*, were computed since the less collimated component reaches the opposite wall of $x^* = 1$ from the wall of $x^* = 0$
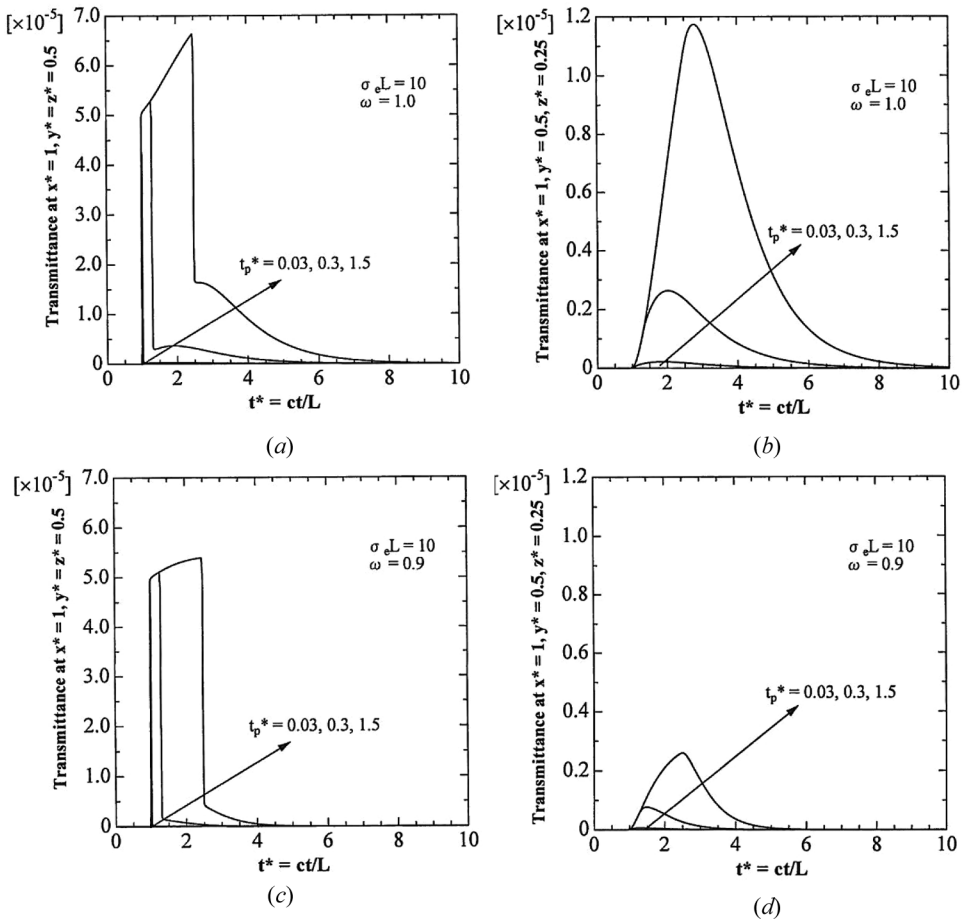

Figure 6. Temporal distributions of transmittance at detectors 3 and 4 for (*a*) and (*b*) $\sigma_e L = 10$, $\omega = 1$, and (*c*) and (*d*) $\sigma_e L = 10$, $\omega = 0.9$, when the spot at $x^* = 0$, $y^* = z^* = 0.5$ of the unit cube was subjected to a single collimated square pulse with various pulse widths of $t_p^* = 0.03$, 0.3, and 1.5.

subjected to a single collimated unit step square pulse for $\sigma_e L = 10$, as well as the depth of the energy deposition for $\sigma_e L = 10$ shown in Figure 3.

The superposition analyses of a single pulse and a pulse train consisting of five identical pulses were investigated as follows. Three different pulse widths and four different pulse train intervals were considered. Figure 5 shows the temporal distributions of transmittance at detectors 3 and 4 for $\sigma_e L = 0.1$, $\omega = 1$, (Figures 5a and 5b) and $\sigma_e L = 0.1$, $\omega = 0.9$ (Figures 5c and 5d), when the spot at $x^* = 0$, $y^* = z^* = 0.5$ of the unit cube is subjected to a single collimated square pulse with various pulse widths of $t_p^* = 0.03$, 0.3, and 1.5. The corresponding figures for optically thick
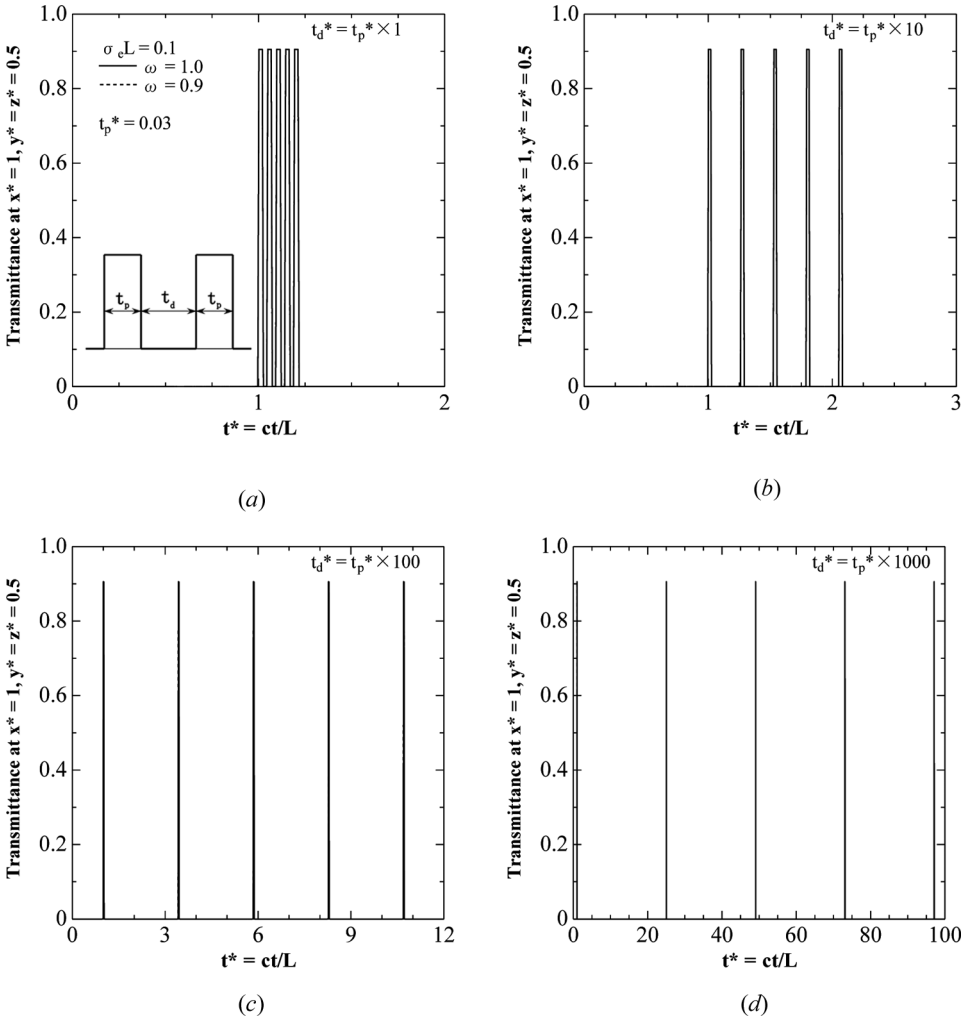

Figure 7. Temporal distributions of transmittance at detector 3 for $\sigma_e L = 0.1$, $\omega = 1$ and 0.9, when the spot at $x^* = 0$, $y^* = z^* = 0.5$ of the unit cube was subjected to a collimated square pulse train consisting of five pulses with constant pulse width of $t_p^* = 0.03$ and various pulse train intervals. (a) $t_d^* = t_p^* \times 1$, (b) $t_d^* = t_p^* \times 10$, (c) $t_d^* = t_p^* \times 100$, and (d) $t_d^* = t_p^* \times 1000$.

medium of $\sigma_e L = 10$ are shown in Figure 6. These results were constructed by the use of the superposition theorem based on the solution of the basic problem subjected to a unit step pulse shown in Figures 4c and 4d. In Figures 5a and 5c at detector 3, it is seen that the magnitude of the transmitted pulse is the same as that for a single collimated unit step square pulse shown in Figure 4c for any value of the pulse width t_p^*, and the width of the transmitted pulse is also the same as t_p^*; in addition, the temporal distributions of transmittance scarcely depend on the scattering albedo. That is, the transmitted pulse is dominated by the collimated component. On the other hand, in Figures 5b and 5d at detector 4, it is seen that the magnitude of transmittance increases with the increase of pulse width. The width of the transmitted pulse
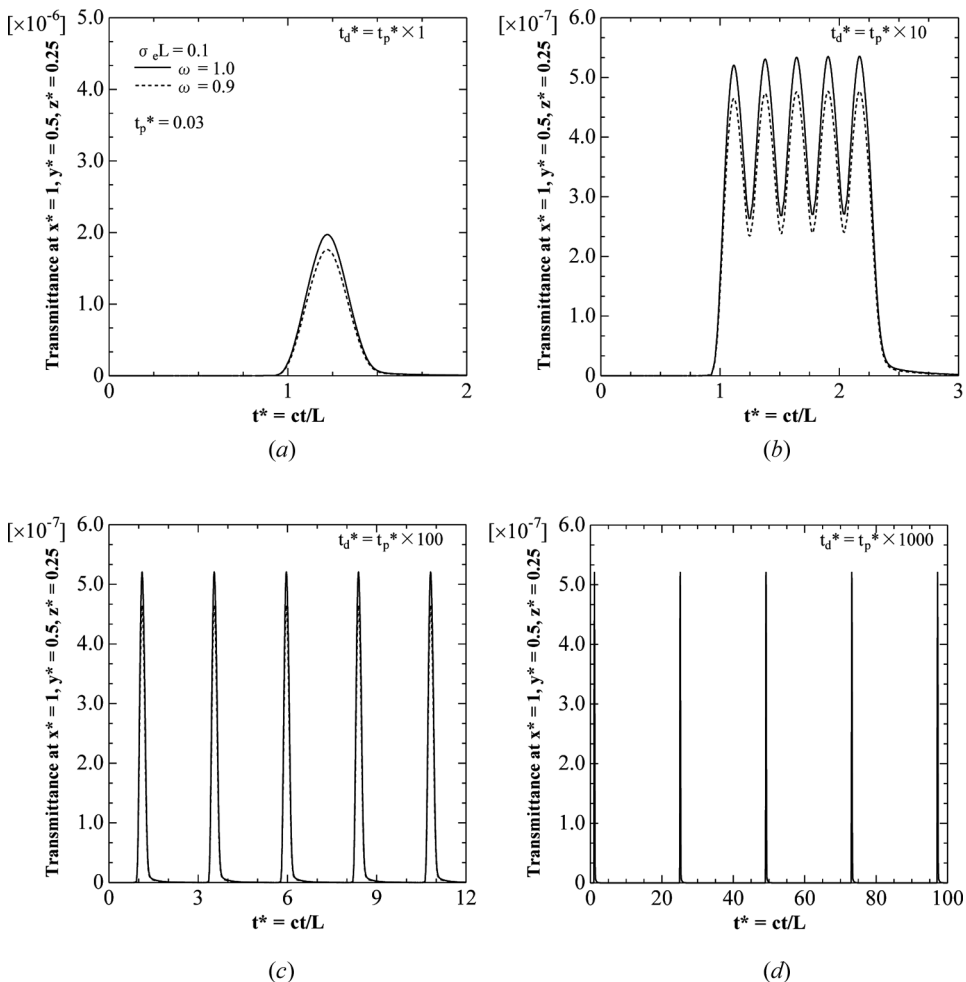

Figure 8. Temporal distributions of transmittance at detector 4 for $\sigma_e L = 0.1$, $\omega = 1$ and 0.9, when the spot at $x^* = 0$, $y^* = z^* = 0.5$ of the unit cube was subjected to a collimated square pulse train consisting of five pulses with constant pulse width of $t_p^* = 0.03$ and various pulse train intervals. (a) $t_d^* = t_p^* \times 1$, (b) $t_d^* = t_p^* \times 10$, (c) $t_d^* = t_p^* \times 100$, and (d) $t_d^* = t_p^* \times 1000$.

is much larger than the incident pulse width t_p^*, and the magnitude of transmittance depends to a slight degree on the scattering albedo. In contrast, for the optically thick medium illustrated in Figure 6, we observed that the broadening of the transmitted pulses becomes larger with the increase of the pulse width for both detector locations, its decaying tail lasts longer, and the magnitude of transmittance strongly depends on the scattering albedo. As is clearly visible in Figures 6a and 6c, although the transmitted pulse is dominated by the collimated component of the irradiation pulse from $t^* = 1$ to $t^* = 1 + t_p^*$, the scattered diffuse radiation contribution builds up gradually from $t^* = 1 + t_p^*$.
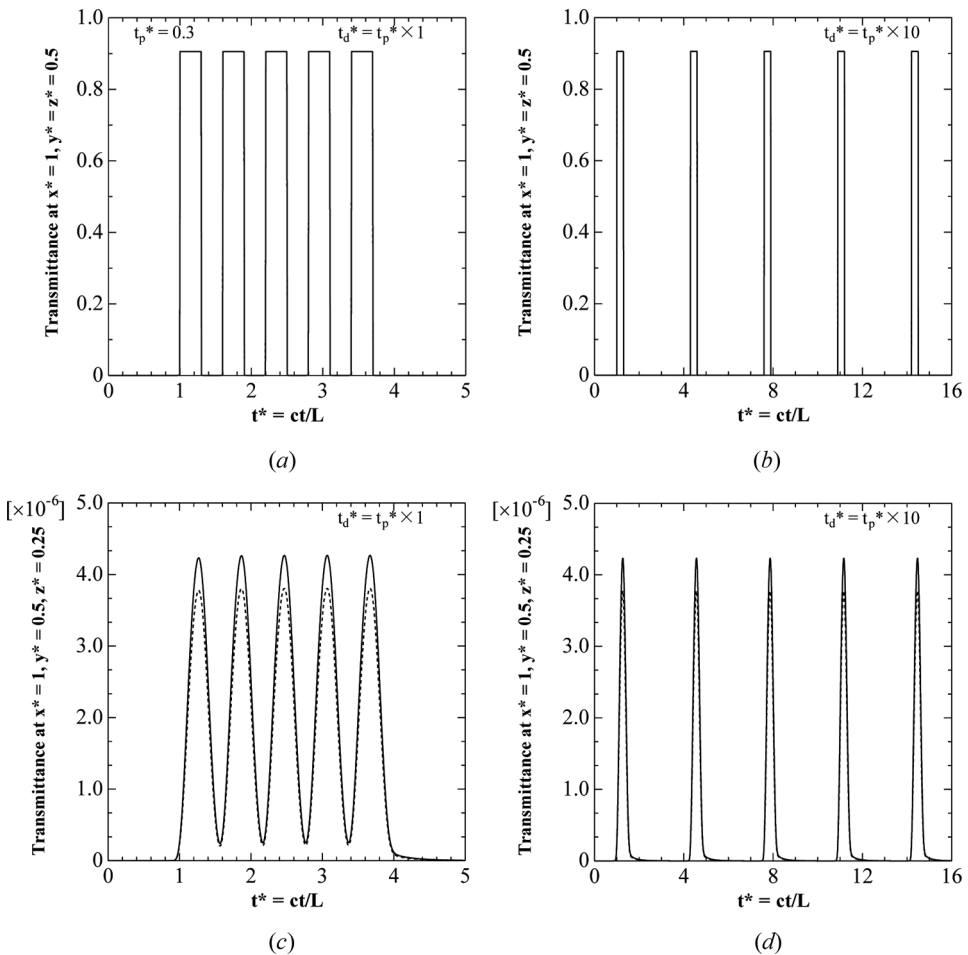

Figure 9. Temporal distributions of transmittance at detectors 3 and 4 for $\sigma_e L = 0.1$, $\omega = 1$ and 0.9, when the spot at $x^* = 0$, $y^* = z^* = 0.5$ of the unit cube was subjected to a collimated square pulse train consisting of five pulses with constant pulse width of $t_p^* = 0.3$ and different pulse train intervals. (a) and (c) $t_d^* = t_p^* \times 1$, (b), and (d) $t_d^* = t_p^* \times 10$.

Figure 7 shows the temporal distributions of transmittance at detector 3 for $\sigma_e L = 0.1$, $\omega = 1$ and 0.9, when the spot at $x^* = 0$, $y^* = z^* = 0.5$ of the unit cube was subjected to a collimated square pulse train consisting of five identical pulses with pulse width of $t_p^* = 0.03$ for four different pulse train intervals ($t_d^* = 1\times$, $10\times, 100\times$, and $1000 \times t_p^*$). The corresponding figures at detector 4 are shown in Figure 8. At detector 3, we found that for any value of the pulse interval t_d^*, the transmittance signals resemble the radiated collimated pulse train in which each individual response matches with that subjected to a single collimated pulse irradiation (shown in Figure 5a). In contrast, at detector 4, the output signal was overlapped despite the irradiation of a train of five pulses in the case $t_d^* = 1 \times t_p^*$ and $10 \times t_p^*$.
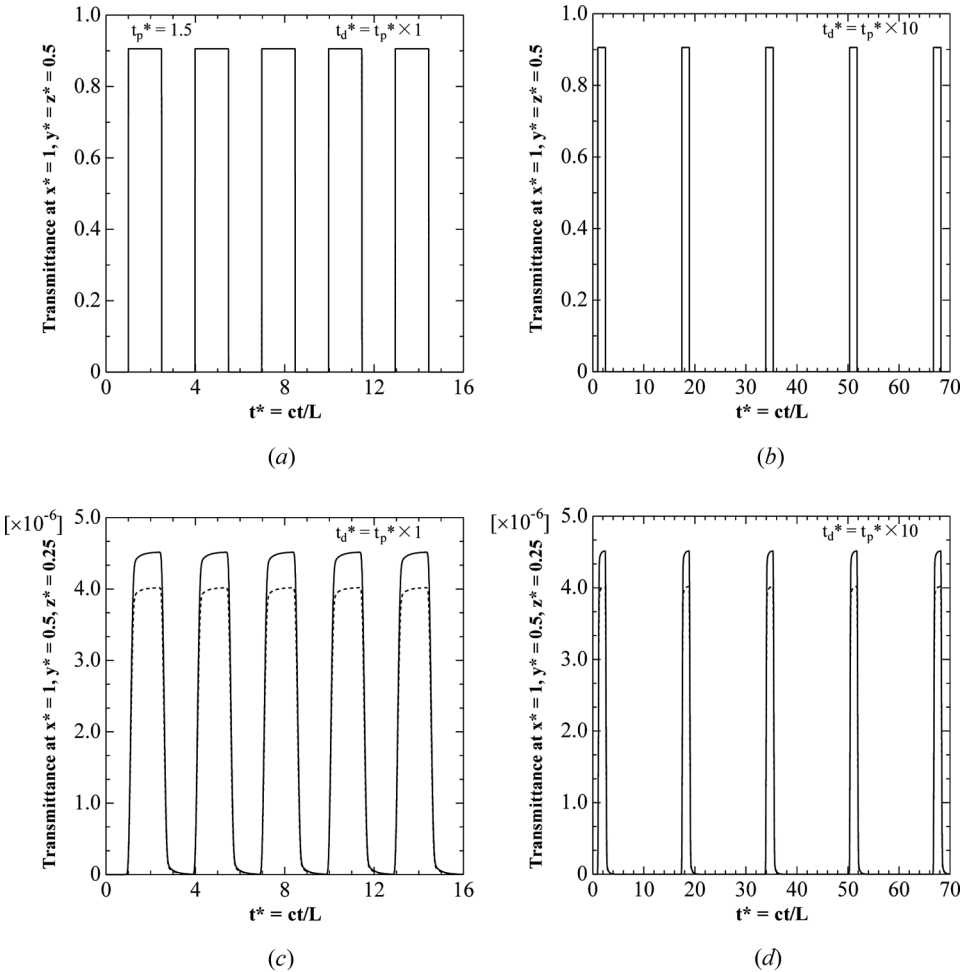

Figure 10. Temporal distributions of transmittance at detectors 3 and 4 for $\sigma_e L = 0.1$, $\omega = 1$ and 0.9, when the spot at $x^* = 0$, $y^* = z^* = 0.5$ of the unit cube was subjected to a collimated square pulse train consisting of five pulses with constant pulse width of $t_p^* = 1.5$ and different pulse train intervals. (a) and (c) $t_d^* = t_p^* \times 1$, (b) and (d) $t_d^* = t_p^* \times 10$.

Under the condition of $t_d^* = 1 \times t_p^*$, the output signal at detector 4 was detected as a single pulse, and the responses of the five pulses are totally superposed. The magnitude of the signal in Figure 8a is about four times larger than that subjected to a single pulse irradiation (shown in Figures 5b and 5d). This is consistent with the findings in our previous study for diffuse irradiation [30]. The non-overlap effect at detector 3 for a pulse train is because of the dominant effect of collimated pulses, such that the diffusely scattered radiation contribution is minimized.

Figure 9 shows the temporal distributions of transmittance at detectors 3 and 4 for $\sigma_e L = 0.1$, $\omega = 1$ and 0.9, when the spot at $x^* = 0$, $y^* = z^* = 0.5$ of the unit cube was subjected to a collimated square pulse train consisting of five identical pulses
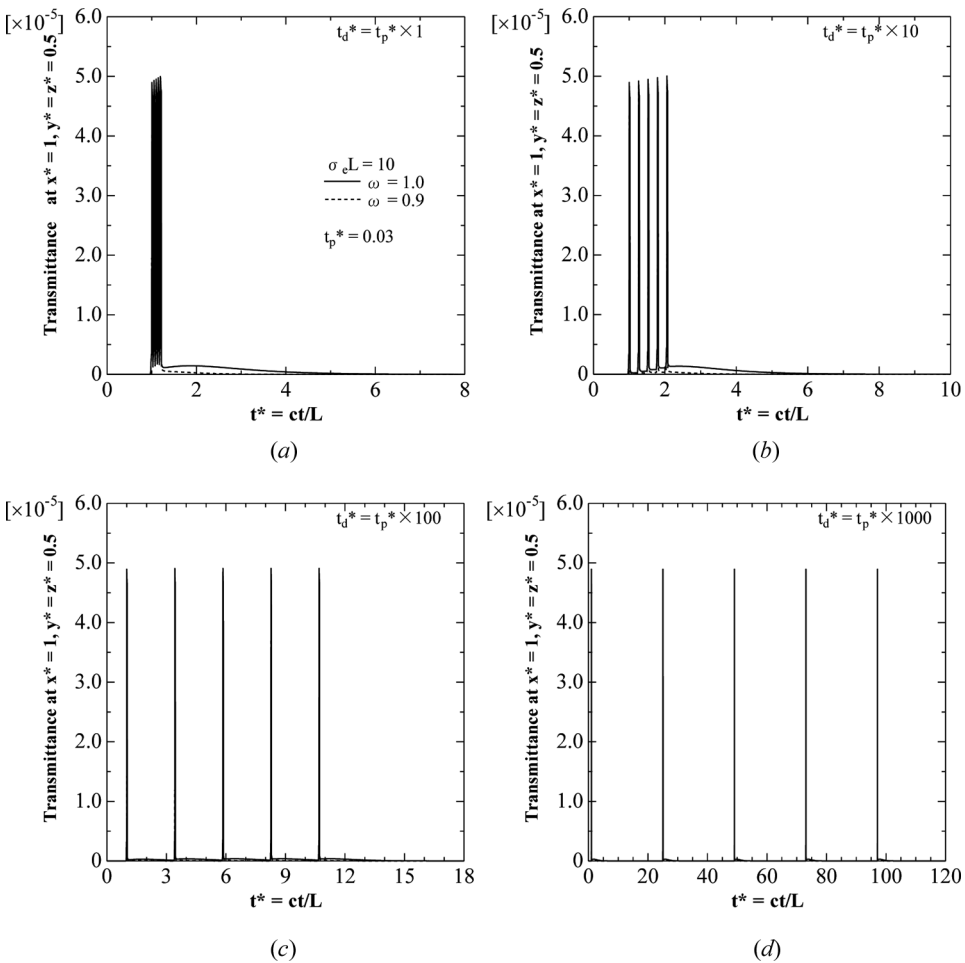

Figure 11. Temporal distributions of transmittance at detector 3 for $\sigma_e L = 10$, $\omega = 1$ and 0.9, when the spot at $x^* = 0$, $y^* = z^* = 0.5$ of the unit cube was subjected to a collimated square pulse train consisting of five pulses with constant pulse width of $t_p^* = 0.03$ and various pulse train intervals. (a) $t_d^* = t_p^* \times 1$, (b) $t_d^* = t_p^* \times 10$, (c) $t_d^* = t_p^* \times 100$, and (d) $t_d^* = t_p^* \times 1000$.

with pulse width of $t_p^* = 0.3$ for two different pulse train intervals ($t_d^* = 1\times$, $10 \times t_p^*$). The corresponding figures for $t_p^* = 1.5$ are shown in Figure 10. The solid line shows that the result for $\omega = 1$, and the dashed line shows that for $\omega = 0.9$. The overlap effect was observed only in Figure 9c for the pulse train with $t_p^* = 0.3$ and $t_d^* = 1 \times t_p^*$. Although it is not presented here, no overlap effect was observed for the pulse trains with $t_p^* = 0.3$, 1.5 and $t_d^* = 100\times$, $1000 \times t_p^*$ at all.

Figures 11–14 show the transmittance signals at detectors 3 and 4 for an optically thick medium of $\sigma_e L = 10$. The results illustrated in these figures show that the overlap effect was observed even at detector 3 when the pulse width and pulse
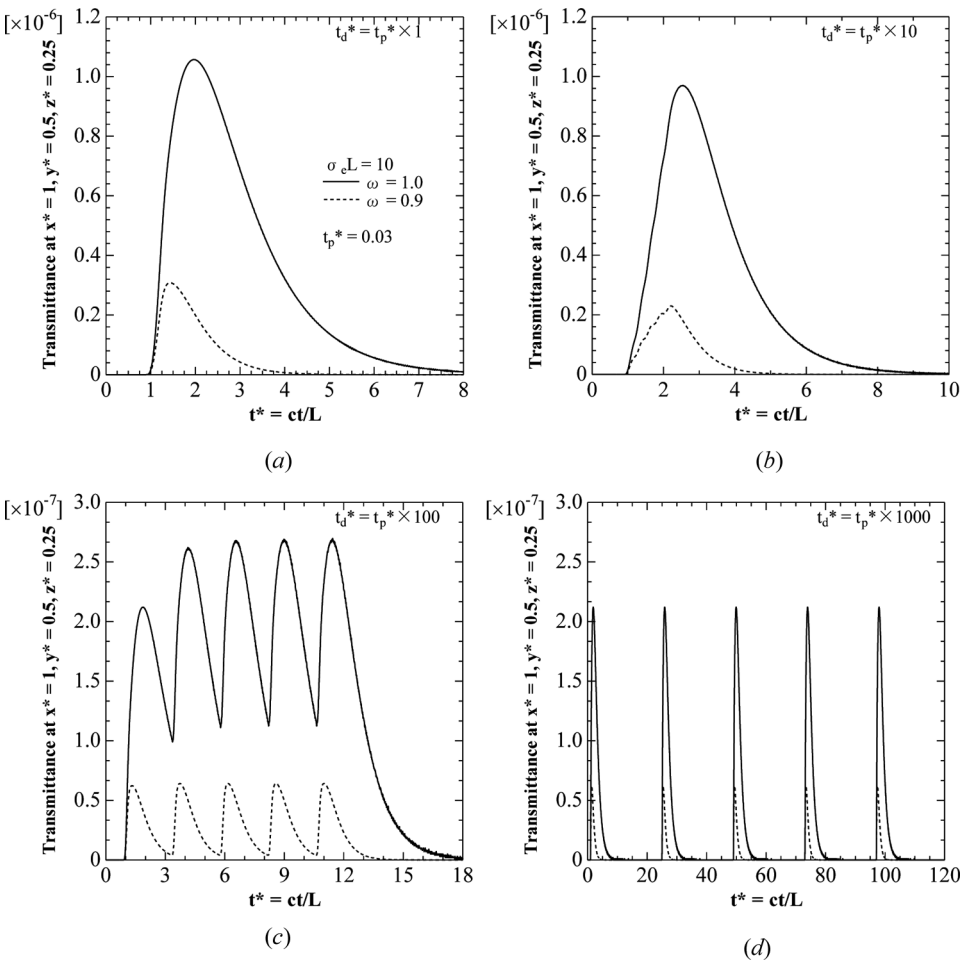

Figure 12. Temporal distributions of transmittance at detector 4 for $\sigma_e L = 10$, $\omega = 1$ and 0.9, when the spot at $x^* = 0$, $y^* = z^* = 0.5$ of the unit cube was subjected to a collimated square pulse train consisting of five pulses with constant pulse width of $t_p^* = 0.03$ and various pulse train intervals. (a) $t_d^* = t_p^* \times 1$, (b) $t_d^* = t_p^* \times 10$, (c) $t_d^* = t_p^* \times 100$, and (d) $t_d^* = t_p^* \times 1000$.

train interval are not appreciable, not to mention at detector 4. The influence of the scattering albedo on the temporal distributions of transmittance was clearly observed at both detectors with the increase of pulse width; while in the case of optically thin medium it was invisible at detector 3. In addition, we found that the peak positions between the responses of the two scattering albedo values were different at detector 4, and the magnitude of the first maximal value became smaller than that of the after-maximal value. Such characteristics were not clearly observed for the optically thin medium. For the pulse train with $t_p^* = 0.3$, 1.5 and $t_d^* = 100\times$, $1000 \times t_p^*$, no overlap effect was found and their results are not shown here.

Figure 13. Temporal distributions of transmittance at detectors 3 and detector 4 for $\sigma_e L = 10$, $\omega = 1$ and 0.9, when the spot at $x^* = 0$, $y^* = z^* = 0.5$ of the unit cube was subjected to a collimated square pulse train consisting of five pulses with constant pulse width of $t_p^* = 0.3$ and different pulse train intervals. (*a*) and (*c*) $t_d^* = t_p^* \times 1$, and (*b*) and (*d*) $t_d^* = t_p^* \times 10$.
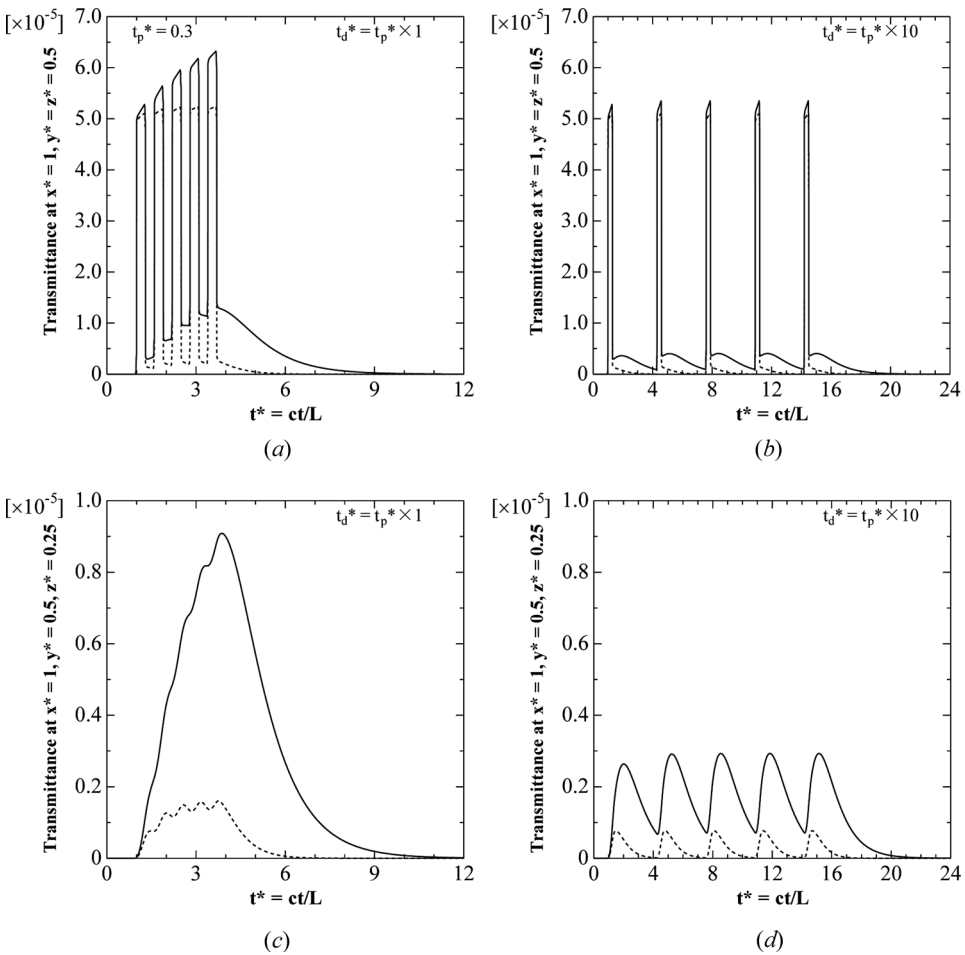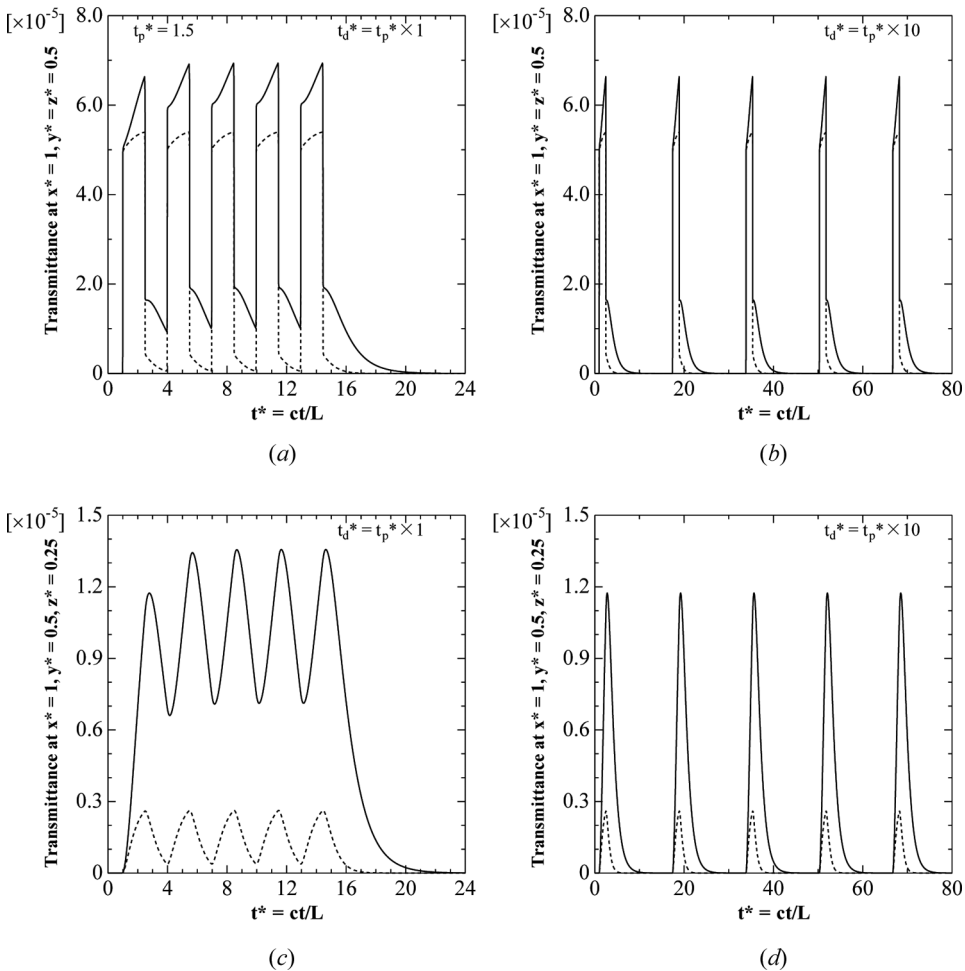
Figure 14. Temporal distributions of transmittance at detectors 3 and 4 for $\sigma_e L = 10$, $\omega = 1$ and 0.9, when the spot at $x^* = 0$, $y^* = z^* = 0.5$ of the unit cube was subjected to a collimated square pulse train consisting of five pulses with constant pulse width of $t_p^* = 1.5$ and different pulse train intervals. (a) and (c) $t_d^* = t_p^* \times 1$, (b) and (d) $t_d^* = t_p^* \times 10$.

CONCLUSION

The transient characteristics of collimated radiative transfer in a scattering-absorbing homogeneous medium cube subjected to a short square pulse train are investigated by applying the transient DOM and Duhamel's superposition theorem. The effects of the optical thickness, the scattering albedo, pulse width, and pulse train interval on the divergence of radiative heat flux, reflectance, and transmittance were examined. Different from diffuse irradiation, the effect of pulse broadening in collimated irradiation is negligible in the region where collimated radiation dominates over the scattered diffuse component; and, thus, the overlap of pulses in the pulse train response is not obvious in such cases. Further, the magnitude of overlap

or superposition effect for a pulse train depends on the compatibility between the pulse interval and the broadening of a single pulse. That is, when the pulse interval is shorter than the broadening, the response of the pulse train overlaps. When the pulse interval is greater than the broadening, the response between two successive pulses does not overlap and distinct individual signals are detectable.

REFERENCES

1. M. S. Patterson, B. Chance, and B. C. Wilson, Time Resolved Reflectance and Transmittance for the Noninvasive Measurement of Tissue Optical Properties, *Appl. Opt.*, vol. 28, pp. 2331–2336, 1989.

2. V. Ntziachristos, A. G. Yodh, M. Schnall, and B. Chance, Concurrent MRI and Diffuse Optical Tomography of Breast After Indocyanine Green Enhancement, *Proc. Natl. Acad. Sci. USA*, vol. 97, pp. 2767–2772, 2000.

3. J. C. Hebden, H. Veenstra, H. Dehghani, E. M. C. Hillman, M. Schweiger, S. R. Arridge, and D. T. Delpy, Three-Dimensional Time-Resolved Optical Tomography of a Conical Breast Phantom, *Appl. Opt.*, vol. 40, pp. 3278–3287, 2001.

4. Y. Yamada, Light-Tissue Interaction and Optical Imaging in Biomedicine, *Annual Rev. Heat Transfer*, vol. 6, pp. 1–59, 1995.

5. H. Quan and Z. Guo, Fast 3-D Optical Imaging with Transient Fluorescence Signals, *Optics Express*, vol. 12, pp. 449–457, 2004.

6. B. Hunter and Z. Guo, Phase-Function Normalization for Accurate Analysis of Ultrafast Collimated Radiative Transfer, *Appl. Opt.*, vol. 51, pp. 2192–2201, 2012.

7. B. Hunter and Z. Guo, Conservation of Asymmetry Factor in Phase Function Discretization for Radiative Transfer Analysis in Anisotropic Scattering Media, *Int. J. Heat Mass Transfer*, vol. 55, pp. 1544–1552, 2012.

8. J. Jiao and Z. Guo, Modeling of Ultrashort Pulsed Laser Ablation in Water and Biological Tissues in Cylindrical Coordinates, *Appl. Phys. B*, vol. 103, pp. 195–205, 2011.

9. H. Huang and Z. Guo, Ultrashort Pulsed Laser Ablation and Stripping of Freeze-Dried Dermis, *Lasers Med. Sci.*, vol. 25, pp. 517–524, 2010.

10. M. Jaunich, S. Raje, K. Kim, K. Mitra, and Z. Guo, Bio-Heat Transfer Analysis during Short Pulse Laser Irradiation of Tissues, *Int. J. Heat Mass Transfer*, vol. 51, pp. 5511–5521, 2008.

11. T. Tanaka, S. Noda, A. Chutinan, T. Asano, and N. Yamamoto, Ultra-Short Pulse Propagation in 3-D GaAs Photonic Crystals, *Opt. Quant. Electronics*, vol. 34, pp. 37–43, 2002.

12. K. Mitra, M.-S. Lai, and S. Kumar, Transient Radiation Transport in Participating Media within a Rectangular Enclosure, *J. Thermophysics Heat Transfer*, vol. 11, pp. 409–414, 1997.

13. Z. Guo, J. Aber, B. A. Garetz, and S. Kumar, Monte Carlo Simulation and Experiments of Pulsed Radiative Transfer, *J. Quantitative Spectros. Radiative Transfer*, vol. 73, pp. 159–168, 2002.

14. C. Y. Wu, Monte Carlo Simulation of Transient Radiative Transfer in a Medium with a Variable Refractive Index, *Int. J. Heat Mass Transfer*, vol. 52, pp. 4151–4159, 2009.

15. Z. Guo and S. Kumar, Three-Dimensional Discrete Ordinates Method in Transient Radiative Transfer, *J. Thermophys. Heat Transfer*, vol. 16, pp. 289–296, 2002.

16. S. C. Mishra, H. K. Roy, and N. Misra, Discrete Ordinate Method with a New and a Simple Quadrature Scheme, *J. Quant. Spectrosc. Radiat. Transfer*, vol. 101, pp. 249–262, 2006.

17. I. Ayranci and N. Selcuk, MOL Solution of DOM for Transient Radiative Transfer in 3-D Scattering Media, *J. Quant. Spectrosc. Radiat. Transfer*, vol. 84, pp. 409–422, 2004.

M. AKAMATSU AND Z. GUO

18. J. C. Chai, P. F. Hsu, and Y. C. Lam, Three-Dimensional Transient Radiative Transfer Modeling using the Finite-Volume Method, *J. Quantitative Spectroscopy Radiative Transfer*, vol. 86, pp. 299–313, 2004.
19. B. Hunter and Z. Guo, Comparison of Discrete-Ordinates Method, and Finite Volume Method for Steady-State, and Ultrafast Radiative Transfer Analysis in Cylindrical Coordinates, *Numer Heat Transfer B*, vol. 59, pp. 339–359, 2011.
20. K. Mitra and S. Kumar, Development and Comparison of Models for Light-Pulse Transport through Scattering–Absorbing Media, *Appl. Opt.*, vol. 38, pp. 188–196, 1999.
21. Z. Guo and S. Kumar, Discrete-Ordinates Solution of Short-Pulsed Laser Transport in Two-Dimensional Turbid Media, *Appl. Optics*, vol. 40, pp. 3156–3163, 2001.
22. K. H. Kim and Z. Guo, Ultrafast Radiation Heat Transfer in Laser Tissue Welding and Soldering, *Numer Heat Transfer A*, vol. 46, pp. 23–40, 2004.
23. C. Y. Wu and N. R. Ou, Differential Approximations for Transient Radiative Transfer through a Participating Medium exposed to Collimated Irradiation, *J. Quantitative Spectroscopy Radiative Transfer*, vol. 73, pp. 111–120, 2002.
24. S. C. Mishra, P. Chugh, P. Kumar, and K. Mitra, Development, and Comparison of the DTM, the DOM and the FVM Formulations for the Short-Pulse Laser Transport through a Participating Medium, *Int. J. Heat Mass Transfer*, vol. 49, pp. 1820–1832, 2006.
25. T. Okutucu and Y. Yener, Radiative Transfer in Participating Media with Collimated Short-Pulse Gaussian Irradiation, *J. Phys. D: Appl. Phys.*, vol. 39, pp. 1976–1983, 2006.
26. R. Muthukumaran and S. C. Mishra, Transient Response of a Planar Participating Medium Subjected to a Train of Short-Pulse Radiation, *Int. J. Heat Mass Transfer*, vol. 51, pp. 2418–2432, 2008.
27. R. Muthukumaran and S. C. Mishra, Effect of a Step Short-Pulse Laser Train on an Inhomogeneous Planar Participating Medium, *Int. Comm. Heat Mass Transfer*, vol. 35, pp. 1073–1078, 2008.
28. R. Muthukumaran and S. C. Mishra, Transport of a Train of Short-Pulse Radiation of Step Temporal Profile through a 2-D Participating Medium, *Int. J. Heat Mass Transfer*, vol. 51, pp. 2282–2298, 2008.
29. R. Muthukumaran and S. C. Mishra, Thermal Signatures of a Localized Inhomogeneity in a 2-D Participating Medium Subjected to an Ultra-Fast Step-Pulse Laser Wave, *J. Quantitative Spectroscopy Radiative Transfer*, vol. 109, pp. 705–726, 2008.
30. M. Akamatsu, and Z. Guo, Ultrafast Radiative Heat Transfer in Three-Dimensional Highly-Scattering Media Subjected to Pulse Train Irradiation, *Numer Heat Transfer A*, vol. 59, pp. 653–671, 2011.
31. Z. Guo and S. Maruyama, Scaling Anisotropic Scattering in Radiative Transfer in Three-Dimensional Nonhomogeneous Media, *Int. Comm. Heat Mass Transfer*, vol. 26, pp. 997–1007, 1999.
32. K. D. Lathrop, Spatial Differencing of the Transport Equation: Positive vs. Accuracy, *J. Comput. Phys.*, vol. 4, pp. 475–498, 1968.